Self-Decoupled Dual Sequence Current Control of D-STATCOM Under Unbalanced Grid Voltage

Xuefeng Wang and Li Peng, *Senior Member, IEEE*

***Abstract*—For the distributed static synchronous compensator (D-STATCOM), the sequence extraction (SE) is generally necessary in dual sequence current controls (DSCCs) based on double synchronous reference frame (SRF), when the D-STATCOM suffers from unbalanced grid voltage. However, the SE will narrow down the control bandwidth and increase the control complexity. In this article, the influences of not using SE on the DSCC are analyzed. On this basis, a self-decoupled dual sequence current control (SDDSCC) is proposed. Accordingly, a novel control parameter design method of SDDSCC is also proposed. The SDDSCC can achieve two types of decoupling. One is the positive and negative sequence current decoupling in double SRF without SE. The other is the *dq* current decoupling without specialized *dq* decoupling method. Due to not using SE and specialized *dq* decoupling method, the control bandwidth of the proposed SDDSCC is larger, and the current dynamic response is faster, and the control structure and implementation are simpler. Besides, the control parameter is easily determined by the novel control parameter design method, without multiple iterations of design. Experimental results verify the proposed scheme.**

***Index Terms*—Control parameter design, decoupling, distributed static synchronous compensator (D-STATCOM), dual sequence current control (DSCC), unbalanced grid voltage.**

I. Introduction

DISTRIBUTED static synchronous compensators (D-STATCOMs) have been employed for voltage regulation, harmonic elimination, power factor correction, and renewable energy grid connection system stability improvement [1], [2], [3], [4].

According to [5], 67% of the grid faults are single-line-to-ground, 25% are line-to-line, 5% are three-phase and three-phase-to-ground and 3% are two-lines-to-ground faults. In the distributed network, the grid impedance is mainly inductive [6]. Therefore, D-STATCOM, photovoltaic inverters and wind power converters are required not only to remain connected to the power grid but also to output a certain positive and negative sequence reactive current to support the grid voltage when unbalanced grid faults occur, which is the low-voltage ride-through (LVRT) capability [7], [8]. Spain, German, and Denmark have already published the LVRT grid codes and reactive current injection requirements for the grid-connected converters in 2008, 2006 and 2004, respectively, [9], [10], [11]. As an example, the German E.ON Netz grid code is shown in Fig. 1 [10]. It can be seen in Fig. 1(a) that only when the grid voltage falls below the red curve, the converter is allowed to disconnected from the grid. Otherwise, it should inject a certain amount of reactive current which is defined in Fig. 1(b). Furthermore, the faster the reactive current is injected, the faster the grid voltage will recover from a fault, which ensures that the LVRT is realized. According to the recently issued German grid code VDE-AR-N 4110 [12] and [13], the positive and negative sequence reactive current references are set to be proportional to the variations of the positive and negative sequence voltage, respectively. Other common positive and negative sequence current reference generation schemes during unbalanced faults can be given in [7], [8], [14], [15], [16], and [17].

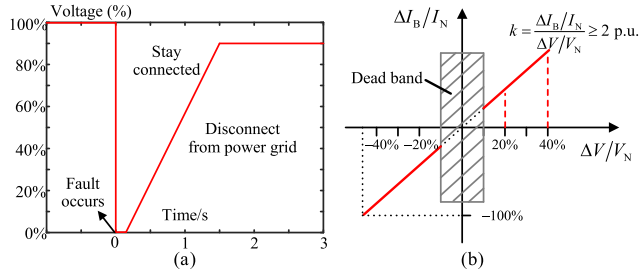

Fig. 1. German grid code requirements. (a) LVRT capability. (b) Reactive current injection requirement.

To fulfill the reference tracking of unbalanced current, different current control schemes are proposed. One common current control is the proportional plus resonant (PR) control, implemented in the stationary reference frame to track the fundamental signal [14], [15], [16], [17], [40]. However, the current references need to be reconstructed into fundamental ac forms by inverse Park transformation, if the active and reactive current references are given in dc forms originally. This will inevitably increase implementation complexity. Besides, ideal PR has the stability issue and is difficult to implement due to the finite precision of digital control system and its effect may suffer from the impact of grid frequency deviation [18], [19]. Another current control scheme is the combination of a proportional integral (PI) controller and a resonant controller, implemented in the single positive sequence SRF or double SRF

Manuscript received 23 August 2023; revised 9 November 2023 and 4 January 2024; accepted 8 February 2024. Date of publication 23 February 2024; date of current version 20 March 2024. Recommended for publication by Associate Editor A. K. Gupta. *(Corresponding author: Li Peng.)*

The authors are with the State Key Laboratory of Advanced Electromagnetic Technology, School of Electrical and Electronic Engineering, Huazhong University of Science and Technology, Wuhan 430074, China (e-mail: xuefeng090@hust.edu.cn; pe105@mail.hust.edu.cn).

Color versions of one or more figures in this article are available at https://doi.org/10.1109/TPEL.2024.3369388.

Digital Object Identifier 10.1109/TPEL.2024.3369388

without sequence extraction (SE) [20], [21], [22]. However, this scheme also has the issue with the complex implementation of the resonant controller. Besides, the *d*-/*q*-axis current reference reconstruction is also needed if the original reference is given in the dc form, which will increase the implementation complexity.

Since active/reactive current can be directly controlled by *d*/*q* current in the SRF, one dual sequence current control (DSCC) based on double SRF is proposed in [23], and each sequence d or *q*-axis adopts one PI controller. Compared with resonant controller, this scheme is simpler in the controller design and digital implementation. In addition, the current reference can be simple dc form and no current reference reconstruction is needed. However, the interaction between current vector and different sequence SRF gives rise to a coupled second harmonic component in each *d*- or *q*-axis. This coupling will lead to the fact that positive and negative sequence current cannot be controlled independently from each other. To achieve the independent control of dual sequences, common sequence component separation methods include notch filter (NF) [23], [24], [25], delay signal cancellation [26], and dual second-order generalized integrator [27], [28], [29]. However, this will increase the control complexity and introduce phase delay and significantly narrow down the current control bandwidth [30]. In [31], a scheme based on the decoupled double SRF is used to suppress the coupled second harmonic component. However, a low-pass digital filter with relatively low cutoff frequency is still needed.

To solve the issues caused by the SE in double SRF, a DSCC without SE is proposed in [32] and [33]. However, in order to eliminate the influences of the coupled second harmonic component, each d or q current reference in double SRF is required to be reconstructed from the original simple dc form to the combination form of a DC component and a second harmonic component through inverse Park transformation, which will inevitably increase the control complexity. Common dc form current reference generation schemes in double SRF under unbalanced grid voltage can be given [38] and [39]. Besides, for suppressing the *dq* coupling in double SRF, a specialized *dq* current decoupling method is generally needed in the current control [23], [24], [25]. However, the *dq* current decoupling effect of the scheme in [32] using current reference feedforward instead of real-time current feedback is limited. In [33], how to solve the *dq* current coupling issue in double SRF was not mentioned.

In this article, the aforementioned problems of the conventional DSCC based on double SRF are planned to be solved under the conditions of no SE and current reference reconstruction. On this basis, the specific influences of no SE on the conventional DSCC are analyzed and clarified. Inspired by the analysis results of the influences, a novel self-decoupled dual sequence current control (SDDSCC) scheme is proposed in this article. Accordingly, a novel control parameter design method of the SDDSCC scheme is also proposed.

The contributions of this article can be shown as follows.

1) The influences of no SE on the conventional DSCC in double SRF are analyzed and clarified. On this basis, the SDDSCC is proposed.
2) The proposed SDDSCC can achieve two types of decoupling. One is the positive and negative sequence current decoupling in double SRF without SE. The other is the *dq* current decoupling in double SRF without specialized *dq* decoupling method.
3) Compared to the conventional scheme with SE, the current dynamic response of the proposed SDDSCC is faster, because no delayed digital filter for SE is used in control loop.
4) The control structure and implementation of the proposed SDDSCC are also simpler, because it does not need SE or specialized *dq* current decoupling or current reference reconstruction.
5) The control parameters of the SDDSCC can be easily determined by the proposed novel control parameter design method without multiple iterations of design.

Experimental results verify the proposed SDDSCC scheme.

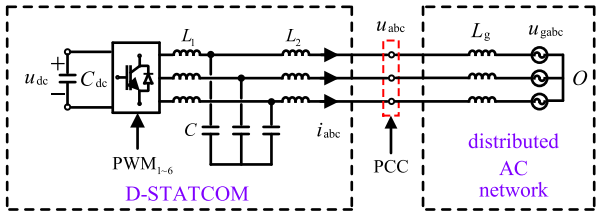

Fig. 2. Circuit of D-STATCOM and AC network.

II. Influences of No Sequence Extraction on Conventional DSCC

Fig. 2 shows the circuit of the D-STATCOM, including a three-phase voltage source inverter, a dc-side capacitor $C_{\rm dc}$, and an *LCL* output filter. In this article, the power grid and other grid-connected inverters at the point of common coupling (PCC), together are equivalent to a Thevenin equivalent voltage source u_{gabc} in series with a grid impedance L_g, as shown in Fig. 2. When the grid voltage u_{gabc} is unbalanced, the voltage u_{abc} at PCC becomes unbalanced accordingly. Unbalanced voltage or current can be decomposed into three balanced components in positive, negative and zero sequence. In a three-phase three-wire system, there is no zero sequence component. In this article, the positive and negative sequence quantities are denoted by subscripts p and n, respectively. The quantities without SE in the positive and negative sequence synchronous reference frame (SRF) are denoted by subscripts pSRF and nSRF, respectively. The quantities in different axes of SRF are distinguished by subscripts d and q, respectively.

A. Conventional DSCC

To eliminate the positive and negative sequence current coupling in conventional DSCC, SE is generally used. However, it will inevitably narrow down the current control bandwidth and increase the control complexity. In this article, the NF is taken as an example to illustrate this issue.

The control block diagram of conventional DSCC based on NF is shown in Fig. 3. The NF can be expressed as

$$G_{\rm NF}(s)=\frac{s^2+\omega_2^2}{s^2+\omega_2 s/Q+\omega_2^2} \tag{1}$$

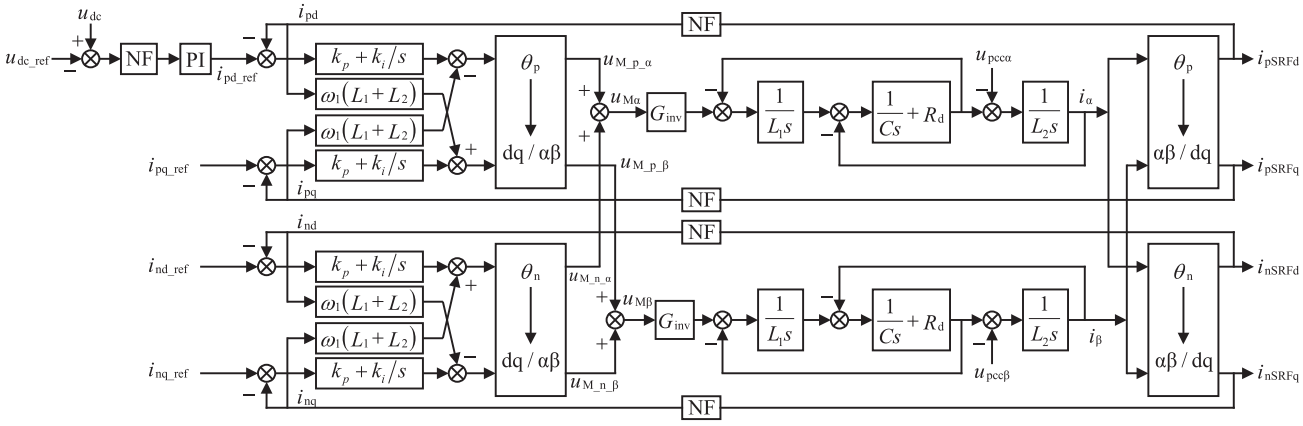

Fig. 3. Control block diagram of conventional DSCC with the NF.

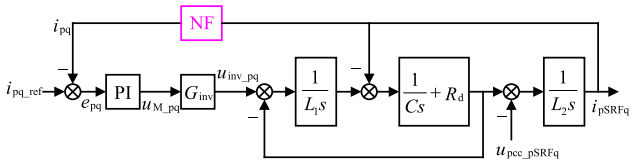

Fig. 4. Positive sequence q axis equivalent control block diagram of conventional DSCC with NF.

where ω_2 is the notch frequency, which is set to twice the fundamental frequency ω_1; and the Q is quality factor, which is set to 0.707 [34].

In Fig. 3, a specialized *dq* current decoupling is used, which includes four $\omega_1(L_1+L_2)$ paths and ignores the high frequency signal coupling path $\omega_1 C$ [35]. u_M is the total modulation reference. θ_p/θ_n is positive/negative sequence coordinate transformation angle, $\theta_p = -\theta_n = \omega_1 t$. θ_p is obtained by locking the phase of the positive sequence voltage in u_{abc}. R_d is a passive resistance used to damp the resonance of *LCL*. According to [35] and [37], the inverter bridge can be expressed as

$$G_{\text{inv}}(s) = e^{-1.5sT_s} \tag{2}$$

where T_s is the sampling period.

The control structures of d and q axis in Fig. 3 are the same after *dq* decoupling. The equivalent block diagram can be illustrated in Fig. 4, which is taking the positive sequence *q*-axis as an example. Then, the open-loop transfer function $G_{\text{op1}}(s)$ of the conventional DSCC with NF can be derived as

$$G_{\text{op1}}(s) = \frac{G_i(s)G_{\text{inv}}(s)(1+sR_dC)G_{\text{NF}}(s)}{s^3L_1L_2C + s^2R_dC(L_1+L_2) + s(L_1+L_2)} \tag{3}$$

where, $G_i(s) = k_p + k_i/s$. k_p and k_i are the proportional and integral parameters, respectively.

Next, with the main circuit parameters in Table I, the bode diagrams of $G_{\text{op1}}(s)$ under different phase margin (PM) are shown in Fig. 12. To find out the influence of NF, the bode diagrams of NF and $G_{\text{op1}}(s)$ without NF are plotted in Fig. 13(a) and 13(b) respectively. In Fig. 12(a) and Fig. 13(b), the PMs of $G_{\text{op1}}(s)$ with and without NF are set to be the same for fair comparison, i.e., 68.3deg around. It can be observed from Figs. 12 and 13 that the bandwidth (ω_c) of $G_{\text{op1}}(s)$ with NF must not exceed the notch frequency $2\omega_1$ of the NF (i.e., 628 rad/s), in order to ensure that PM is greater than 0. Furthermore, the larger the PM, the narrower the bandwidth. Therefore, the NF or other SE method will narrow down the bandwidth of conventional DSCC, and consequently slow down the current dynamic response.

In addition, four SE modules and four *dq* current decoupling paths are needed in the conventional DSCC scheme, as shown in Fig. 3. This will increase the control complexity.

TABLE I
EXPERIMENTAL PARAMETERS

Parameter	Symbol	Value
DC-link voltage	U_{dc}	450 V
AC voltage (phase-phase rms)	U_g	210 V
Power rating	P_0	7.7 kW
Grid frequency	f_0	50 Hz
Transformer inductance	L_g	0.45 mH
Converter-side inductor of *LCL*	L_1	1.0 mH
Capacitor of *LCL*	C	9 uF
Grid-side inductor of *LCL*	L_2	0.6 mH
Resistor in series with *C* of *LCL*	R_d	1 Ω
Sampling frequency	f_s	9.6 kHz

B. Influences of No Sequence Extraction on Conventional DSCC

As explained in Section II-A, the use of SE narrows down the control bandwidth of conventional DSCC. Then, one would wonder what the influences of the positive and negative sequence current coupling would be if no SE is used in the conventional DSCC. Therefore, in this part, the influences of not using SE will be analyzed and clarified.

As shown in Fig. 3, if no SE is used in the conventional DSCC, the feedback currents change from i_{pd}, i_{pq}, i_{nd} and i_{nq} to $i_{p\text{SRF}\,d}$, $i_{p\text{SRF}\,q}$, $i_{n\text{SRF}\,d}$ and $i_{n\text{SRF}\,q}$, respectively. $i_{p\text{SRF}\,d}$ and $i_{p\text{SRF}\,q}$ are the direct *dq* quantities of $i_{\alpha\beta}$ after the positive sequence Park transformation, and they contain both the dc component and the coupled second harmonic component because no SE is used.

The same goes for $i_{n\mathrm{SRF}\,d}$ and $i_{n\mathrm{SRF}\,q}$. If SE is used, i_{pd} and i_{pq} are the *dq* components of the positive sequence component of $i_{\alpha\beta}$ after positive sequence Park transformation, and they contain only dc components. The same goes for i_{nd} and i_{nq}. The relationship between these two kinds of quantities can be expressed as

$$\begin{bmatrix} i_{p\mathrm{SRF}d} \\ i_{p\mathrm{SRF}q} \end{bmatrix} = \begin{bmatrix} i_{pd} \\ i_{pq} \end{bmatrix} + \begin{bmatrix} i_{p\mathrm{SRF}d2\omega} \\ i_{p\mathrm{SRF}q2\omega} \end{bmatrix} \tag{4}$$

$$\begin{bmatrix} i_{n\mathrm{SRF}d} \\ i_{n\mathrm{SRF}q} \end{bmatrix} = \begin{bmatrix} i_{nd} \\ i_{nq} \end{bmatrix} + \begin{bmatrix} i_{n\mathrm{SRF}d2\omega} \\ i_{n\mathrm{SRF}q2\omega} \end{bmatrix} \tag{5}$$

where,

$$\begin{bmatrix} i_{p\mathrm{SRF}d2\omega} \\ i_{p\mathrm{SRF}q2\omega} \end{bmatrix} = \begin{bmatrix} \cos 2\omega_1 t & \sin 2\omega_1 t \\ -\sin 2\omega_1 t & \cos 2\omega_1 t \end{bmatrix} \begin{bmatrix} i_{nd} \\ i_{nq} \end{bmatrix} \tag{6}$$

$$\begin{bmatrix} i_{n\mathrm{SRF}d2\omega} \\ i_{n\mathrm{SRF}q2\omega} \end{bmatrix} = \begin{bmatrix} \cos 2\omega_1 t & -\sin 2\omega_1 t \\ \sin 2\omega_1 t & \cos 2\omega_1 t \end{bmatrix} \begin{bmatrix} i_{pd} \\ i_{pq} \end{bmatrix}. \tag{7}$$

Therefore, $i_{p\mathrm{SRF}\,d}$, $i_{p\mathrm{SRF}\,q}$, $i_{n\mathrm{SRF}\,d}$ and $i_{n\mathrm{SRF}\,q}$ contain both the dc components (i_{pd}, i_{pq}, i_{nd}, i_{nq}) and the coupled second harmonic components ($i_{p\mathrm{SRF}\,d2\omega}$, $i_{p\mathrm{SRF}\,q2\omega}$, $i_{n\mathrm{SRF}\,d2\omega}$, $i_{n\mathrm{SRF}\,q2\omega}$), when no SE is used. The current reference remains dc form. The error between the current reference and the dc component of the feedback current will be fed into the PI controller.

Similarly, the error between 0 and coupled second harmonic component of the feedback current will also be fed into the PI controller, and then the output quantities will be superimposed on the modulation reference in *p*SRF and *n*SRF, respectively, and they can be derived as

$$\begin{bmatrix} u_{\mathrm{PI}\_p\mathrm{SRF}d2\omega} \\ u_{\mathrm{PI}\_p\mathrm{SRF}q2\omega} \end{bmatrix} = k_p \begin{bmatrix} -i_{p\mathrm{SRF}d2\omega} \\ -i_{p\mathrm{SRF}q2\omega} \end{bmatrix} + k_i \int \begin{bmatrix} -i_{p\mathrm{SRF}d2\omega} \\ -i_{p\mathrm{SRF}q2\omega} \end{bmatrix} dt \tag{8}$$

$$\begin{bmatrix} u_{\mathrm{PI}\_n\mathrm{SRF}d2\omega} \\ u_{\mathrm{PI}\_n\mathrm{SRF}q2\omega} \end{bmatrix} = k_p \begin{bmatrix} -i_{n\mathrm{SRF}d2\omega} \\ -i_{n\mathrm{SRF}q2\omega} \end{bmatrix} + k_i \int \begin{bmatrix} -i_{n\mathrm{SRF}d2\omega} \\ -i_{n\mathrm{SRF}q2\omega} \end{bmatrix} dt. \tag{9}$$

The results of (8) in *p*SRF and (9) in *n*SRF can be converted to *n*SRF and *p*SRF, respectively. This can be done by two coordinate transformations. The first is from *p*SRF/*n*SRF to stationary reference ($\alpha\beta$) frame. The second is from $\alpha\beta$ frame to *n*SRF/*p*SRF. Therefore, the result of (8) in *p*SRF can be converted to *n*SRF, which can be derived as

$$\begin{bmatrix} u_{\mathrm{PI}\_p\mathrm{SRF}2\omega\_n\mathrm{SRF}d} \\ u_{\mathrm{PI}\_p\mathrm{SRF}2\omega\_n\mathrm{SRF}q} \end{bmatrix} = \begin{bmatrix} \cos\omega_1 t & -\sin\omega_1 t \\ \sin\omega_1 t & \cos\omega_1 t \end{bmatrix}^2 \begin{bmatrix} u_{\mathrm{PI}\_p\mathrm{SRF}d2\omega} \\ u_{\mathrm{PI}\_p\mathrm{SRF}q2\omega} \end{bmatrix}. \tag{10}$$

Similarly, the result of (9) in *n*SRF can be converted to the result in *p*SRF, which is

$$\begin{bmatrix} u_{\mathrm{PI}\_n\mathrm{SRF}2\omega\_p\mathrm{SRF}d} \\ u_{\mathrm{PI}\_n\mathrm{SRF}2\omega\_p\mathrm{SRF}q} \end{bmatrix} = \begin{bmatrix} \cos\omega_1 t & \sin\omega_1 t \\ -\sin\omega_1 t & \cos\omega_1 t \end{bmatrix}^2 \begin{bmatrix} u_{\mathrm{PI}\_n\mathrm{SRF}d2\omega} \\ u_{\mathrm{PI}\_n\mathrm{SRF}q2\omega} \end{bmatrix}. \tag{11}$$

Then, by combing (6)–(11), the results can be derived as

$$\begin{bmatrix} u_{\mathrm{PI}\_p\mathrm{SRF}2\omega\_n\mathrm{SRF}d} \\ u_{\mathrm{PI}\_p\mathrm{SRF}2\omega\_n\mathrm{SRF}q} \end{bmatrix} = \begin{bmatrix} -k_p & \frac{k_i}{2\omega_1} \\ -\frac{k_i}{2\omega_1} & -k_p \end{bmatrix} \begin{bmatrix} i_{nd} \\ i_{nq} \end{bmatrix} \tag{12}$$

$$\begin{bmatrix} u_{\mathrm{PI}\_n\mathrm{SRF}2\omega\_p\mathrm{SRF}d} \\ u_{\mathrm{PI}\_n\mathrm{SRF}2\omega\_p\mathrm{SRF}q} \end{bmatrix} = \begin{bmatrix} -k_p & -\frac{k_i}{2\omega_1} \\ \frac{k_i}{2\omega_1} & -k_p \end{bmatrix} \begin{bmatrix} i_{pd} \\ i_{pq} \end{bmatrix}. \tag{13}$$

From (12), it can be seen that an extra quantity of negative $k_p i_{nd}$/$k_p i_{nq}$ is introduced into the *d*-/*q*-axis modulation reference in *n*SRF, respectively. Similarly, from (13), it can be seen that an extra quantity of negative $k_p i_{pd}$/$k_p i_{pq}$ is introduced into the *d*-/*q*-axis modulation reference in *p*SRF, respectively. In addition, it can also be seen that four extra *dq* coupling factors ($k_i/2\omega_1$ or $-k_i/2\omega_1$) are introduced, which are between i_{pd} and i_{pq}, and between i_{nd} and i_{nq}.

If the *dq* current decoupling method remains unchanged when no SE is used, the coupled second harmonic component of the feedback current will also be fed into the *dq* current decoupling algorithm, besides the dc component.

First, the *dq* decoupling output of the dc component of the feedback current is derived as

$$\begin{bmatrix} u_{dCp\_p\mathrm{SRF}d\_\mathrm{DC}} \\ u_{dCp\_p\mathrm{SRF}q\_\mathrm{DC}} \end{bmatrix} = \omega_1(L_1+L_2) \begin{bmatrix} -i_{pq} \\ i_{pd} \end{bmatrix} \tag{14}$$

$$\begin{bmatrix} u_{dCp\_n\mathrm{SRF}d\_\mathrm{DC}} \\ u_{dCp\_n\mathrm{SRF}q\_\mathrm{DC}} \end{bmatrix} = \omega_1(L_1+L_2) \begin{bmatrix} i_{nq} \\ -i_{nd} \end{bmatrix} \tag{15}$$

where the subscript *dCp* refers to the *dq* decoupling output.

Then, the *dq* decoupling output of the coupled second harmonic component of the feedback current can be derived as

$$\begin{bmatrix} u_{dCp\_p\mathrm{SRF}d2\omega} \\ u_{dCp\_p\mathrm{SRF}q2\omega} \end{bmatrix} = \omega_1(L_1+L_2) \begin{bmatrix} -i_{p\mathrm{SRF}q2\omega} \\ i_{p\mathrm{SRF}d2\omega} \end{bmatrix} \tag{16}$$

$$\begin{bmatrix} u_{dCp\_n\mathrm{SRF}d2\omega} \\ u_{dCp\_n\mathrm{SRF}q2\omega} \end{bmatrix} = \omega_1(L_1+L_2) \begin{bmatrix} i_{n\mathrm{SRF}q2\omega} \\ -i_{n\mathrm{SRF}d2\omega} \end{bmatrix}. \tag{17}$$

Similar to (10), the result (16) in *p*SRF can be converted to *n*SRF through two coordinate transformations, yields

$$\begin{bmatrix} u_{dCp\_p\mathrm{SRF}2\omega\_n\mathrm{SRF}d} \\ u_{dCp\_p\mathrm{SRF}2\omega\_n\mathrm{SRF}q} \end{bmatrix} = \begin{bmatrix} \cos\omega_1 t & -\sin\omega_1 t \\ \sin\omega_1 t & \cos\omega_1 t \end{bmatrix}^2 \begin{bmatrix} u_{dCp\_p\mathrm{SRF}d2\omega} \\ u_{dCp\_p\mathrm{SRF}q2\omega} \end{bmatrix}. \tag{18}$$

Similar to (11), the result of (17) in *n*SRF can be converted to *p*SRF, which is derived as

$$\begin{bmatrix} u_{dCp\_n\mathrm{SRF}2\omega\_p\mathrm{SRF}d} \\ u_{dCp\_n\mathrm{SRF}2\omega\_p\mathrm{SRF}q} \end{bmatrix} = \begin{bmatrix} \cos\omega_1 t & \sin\omega_1 t \\ -\sin\omega_1 t & \cos\omega_1 t \end{bmatrix}^2 \begin{bmatrix} u_{dCp\_n\mathrm{SRF}d2\omega} \\ u_{dCp\_n\mathrm{SRF}q2\omega} \end{bmatrix}. \tag{19}$$

By combing (6), (7), (16)–(19), the results can be derived as

$$\begin{bmatrix} u_{dCp\_p\mathrm{SRF}2\omega\_n\mathrm{SRF}d} \\ u_{dCp\_p\mathrm{SRF}2\omega\_n\mathrm{SRF}q} \end{bmatrix} = \omega_1(L_1+L_2) \begin{bmatrix} -i_{nq} \\ i_{nd} \end{bmatrix} \tag{20}$$

$$\begin{bmatrix} u_{dCp\_n\mathrm{SRF}2\omega\_p\mathrm{SRF}d} \\ u_{dCp\_n\mathrm{SRF}2\omega\_p\mathrm{SRF}q} \end{bmatrix} = \omega_1(L_1+L_2) \begin{bmatrix} i_{pq} \\ -i_{pd} \end{bmatrix}. \tag{21}$$

By comparing (21) with (14), and (20) with (15), it can be found that the d/q conversion result is exactly opposite to the *d*/*q* decoupling output of the dc component of the feedback current respectively. This will make the total *d*/*q* decoupling output zero, both in *p*SRF and *n*SRF. Therefore, this specialized *dq* current decoupling method is ineffective, when no SE is used in the conventional DSCC.

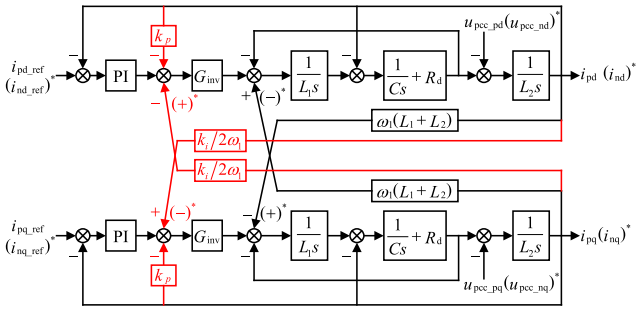

Fig. 5. Positive (negative)∗ sequence equivalent block diagram of conventional DSCC without SE and specialized *dq* decoupling method.

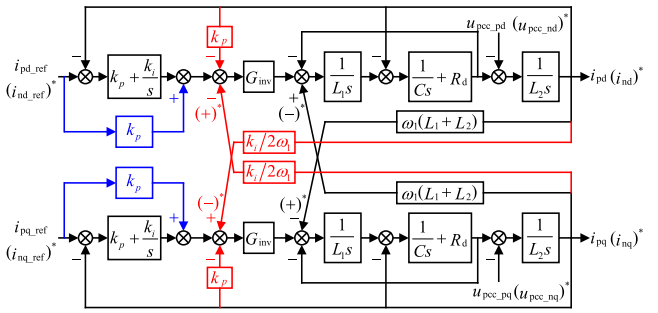

Fig. 6. Positive (negative)∗ sequence equivalent block diagram of proposed SDDSCC without SE and specialized *dq* decoupling method.

With (12), (13) and the ineffectiveness of the specialized *dq* decoupling method, the equivalent positive (or negative) sequence block diagram of conventional DSCC without SE and specialized *dq* decoupling can be illustrated in Fig. 5.

To find out the influence of the extra introduced k_p negative feedback path in Fig. 5, the open loop transfer function $G_{\mathrm{op2}}(s)$ of Fig. 5 is derived as

$$G_{\mathrm{op2}}(s)=\frac{(k_p+k_i/s)G_{\mathrm{inv}}(s)(1+sR_dC)}{\left\{\begin{array}{c}s^3L_1L_2C+s^2R_dC(L_1+L_2)+\\ s[k_pR_dCG_{\mathrm{inv}}(s)+L_1+L_2]+k_pG_{\mathrm{inv}}(s)\end{array}\right\}}. \tag{22}$$

Then, the bode diagrams of $G_{\mathrm{op2}}(s)$ under two different k_p can be plotted in Fig. 14. It can be seen from Fig. 14(a) and (b) that the gain margin (GM) and PM of $G_{\mathrm{op2}}(s)$ are seriously affected by the extra k_p negative feedback path. Instability may even occur under a slightly larger control bandwidth or a slightly larger k_p. Besides, the amplitude-frequency response curves of $G_{\mathrm{op2}}(s)$ drop to 0dB at about 10^2 rad/s and then keep staying around 0dB at the frequency band of $10^2\sim10^4$ rad/s, which means that the control bandwidth is also greatly narrowed down.

In summary, the influences of no SE on the conventional DSCC scheme are shown as follows.

1) An extra quantity of negative k_pi_{nd}/k_pi_{nq} is introduced into the *d*-/*q*-axis modulation reference in *n*SRF, respectively. Similarly, an extra quantity of negative k_pi_{pd}/k_pi_{pq} is introduced into the *d*-/*q*-axis modulation reference in *p*SRF, respectively. This extra quantity will narrow down the control bandwidth greatly. It can cause system instability in case of large k_p.
2) Four extra *dq* coupling factors ($k_i/2\omega_1$ or $-k_i/2\omega_1$) are introduced, which are between i_{pd} and i_{pq}, and between i_{nd} and i_{nq}. This increases the *dq* coupling besides the already existing *dq* coupling of $\omega_1(L_1+L_2)$.
3) The conventional *dq* decoupling method is ineffective.

III. Self-Decoupled Dual Sequence Current Control

A. Self-Decoupled Dual Sequence Current Control

In order to eliminate the three influences of no SE on the conventional DSCC, a SDDSCC is proposed in this section. Firstly, the positive (negative) sequence equivalent control block diagram of the proposed SDDSCC without SE and specialized *dq* decoupling method can be shown in Fig. 6 and the control idea is explained as follows.

Inspired by Fig. 5, a novel k_p current reference feedforward path is proposed to be added to the control structure and the feedforward output is superimposed onto the modulation wave, as shown in Fig. 6. The purpose is to offset the adverse influence of the extra introduced k_p negative feedback path (i.e., $k_pi_{nd}/k_pi_{nq}/k_pi_{pd}/k_pi_{pq}$) caused by not using the SE. From Fig. 6, it can be seen that the two paths (i.e., the proposed k_p current reference feedforward path and the extra introduced k_p negative feedback path) can be merged into one path, which is actually one new proportional control (k_p) for the current error besides the already existing PI (i.e., k_p+k_i/s) control. Therefore, the equivalent combined PI control for the current error can be derived as $2k_p+k_i/s$. In this way, the influence of the extra k_p negative feedback path can be eliminated, and the equivalent control of each *d*-/*q*-axis is still PI control, but the equivalent combined PI controller is $2k_p+k_i/s$, not the original k_p+k_i/s.

On the other hand, by observing the coupling paths between the *d*- and *q*-axis in the equivalent block diagram of Figs. 5 or 6, it can be found that the sign of the already existing *dq* coupling factor $\omega_1(L_1+L_2)$ is exactly opposite to that of the extra introduced *dq* coupling factor $k_i/2\omega_1$ caused by not using SE, in each equivalent *d*- or *q*-axis. Therefore, both the extra introduced coupling path of $k_i/2\omega_1$ and the original coupling path of $\omega_1(L_1+L_2)$ between the *d*- and *q*-axis can be completely eliminated through making the coupling factor $k_i/2\omega_1$ equal to $\omega_1(L_1+L_2)$. In this way, the integral parameter k_i can then be determined by solving the equation of $k_i/2\omega_1=\omega_1(L_1+L_2)$, which is derived as

$$k_i=2\omega_1^2(L_1+L_2). \tag{23}$$

As a result, (23) is an important part of the proposed novel control parameter design method of SDDSCC in this article. The design of proportional parameter k_p will be proposed in the next part.

The above is the main idea of the SDDSCC. Without SE and specialized *dq* decoupling method, the proposed SDDSCC can achieve two types of decoupling at the same time. One is the positive and negative sequence current decoupling. The other is the *dq* current decoupling.

The actual implementation control block diagram of the SDDSCC scheme can be shown in Fig. 7. By comparing Fig. 7

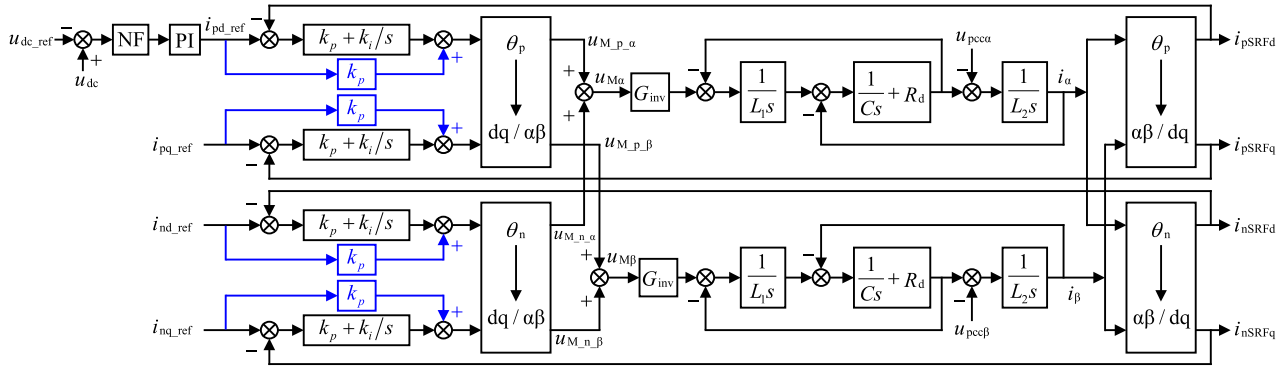

Fig. 7. Implementation block diagram of the proposed SDDSCC scheme.

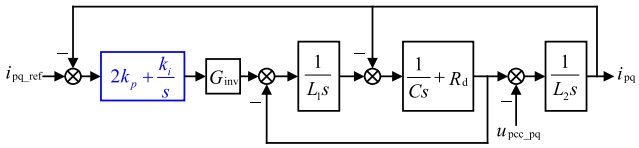

Fig. 8. Positive sequence q-axis equivalent block diagram of SDDSCC.

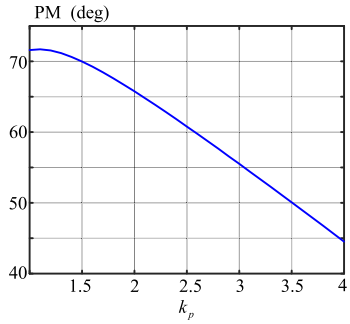

Fig. 9. Relationship graphic of PM and k_p under k_i, T_s, L_1, C, and L_2 known.

with Fig. 3, it can be seen that the conventional scheme has four more SE modules and four more dq current decoupling paths than the proposed SDDSCC scheme. The current reference feedforward in SDDSCC is simple and easy to implement. Therefore, the control structure and implementation of the proposed SDDSCC are simpler than the conventional DSCC with NF.

B. Control Parameter Design of SDDSCC

The design of integral parameter k_i can be referred to (23), and the design of k_p is as follows.

As explained in Section III-A, the equivalent combined PI control of SDDSCC in each d-/q-axis can be derived as $2k_p+k_i/s$. Furthermore, with k_i designed by referring to (23), the dq current coupling of Fig. 6 can be eliminated. Therefore, the further equivalent control block diagram of SDDSCC can be shown in Fig. 8, which is taking the positive sequence q-axis as an example because each sequence d- or q-axis has the same structure.

According to Fig. 8, the open-loop transfer function $G_{\mathrm{op3}}(\mathrm{s})$ of proposed SDDSCC can be expressed as

$$G_{\mathrm{op3}}(s) = \frac{(2k_p + k_i/s)G_{\mathrm{inv}}(s)(1 + sR_dC)}{s^3L_1L_2C + s^2R_dC(L_1 + L_2) + s(L_1 + L_2)}. \tag{24}$$

The resonance angular frequency ω_r of the LCL filter can be derived as

$$\omega_r = \sqrt{\frac{L_1 + L_2}{L_1L_2C}}. \tag{25}$$

Since the gain crossover angular frequency ω_c is lower than ω_r, the influence of the capacitor of LCL filter can be ignored when calculating the magnitude of the open-loop transfer function at ω_c and the angular frequencies lower than ω_c [36]. Thus the magnitude of $G_{\mathrm{op3}}(\mathrm{s})$ can be approximated as

$$|G_{\mathrm{op3}}(s)| \approx \left|\frac{2k_p + k_i/s}{s(L_1 + L_2)}\right|. \tag{26}$$

To avoid the decrease of PM resulted from PI controller, the corner angular frequency $k_i/(2k_p)$ is suggested to be set sufficiently lower than ω_c, which is generally satisfied according to (23). Thus, the PI controller is reduced to a pure proportional gain at ω_c and the frequencies higher than ω_c. Then, by ignoring k_i in (26), k_p is derived as

$$k_p \approx \frac{\omega_c(L_1 + L_2)}{2}. \tag{27}$$

The PM of $G_{\mathrm{op3}}(\mathrm{s})$ can be expressed as

$$\mathrm{PM} = 180^{\circ} + \angle G_{\mathrm{op3}}(s)|_{s=j\omega_c}. \tag{28}$$

Substituting (2) and (25) into (28), yields

$$\mathrm{PM} = \arctan\frac{\omega_r^2 - \omega_c^2}{\omega_c\omega_r^2R_{\mathrm{d}}C} - \arctan\frac{k_i}{2k_p\omega_c} - 1.5T_s\omega_c + \arctan\omega_cR_dC. \tag{29}$$

By substituting (23) and (27) into (29), the relationship between PM and k_p can be obtained, and the relationship graph is plotted in Fig. 9. Therefore, with an expected PM, k_p can be determined by Fig. 9, and this specific k_p is denoted as k_{p_PM}.

For stability, $G_{\mathrm{op3}}(\mathrm{s})$ generally have a positive GM. The bode diagrams of $G_{\mathrm{op3}}(\mathrm{s})$ with and without PI controller are depicted in Fig. 10. As seen, the PI controller only affects the magnitude

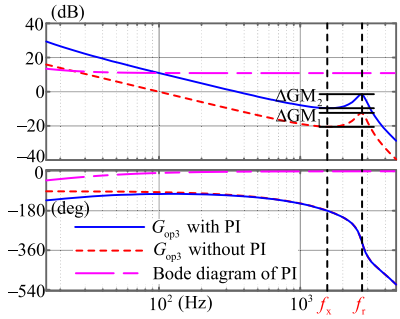

Fig. 10. Bode diagram of $G_{op3}(s)$, with and without PI.

of $G_{op3}(s)$ but not the phase, at the frequencies higher than ω_c. Therefore, the phase crossover frequency f_x of $G_{op3}(s)$ remains unchanged, whether with or without PI controller, as shown in Fig. 10. Furthermore, the magnitude increment between f_x and f_r ($f_r = \omega_r/2\pi$) is also unchanged, with or without PI, i.e., $\Delta GM_1 \approx \Delta GM_2$ in Fig. 10. Due to $G_{inv}(s)$, it is difficult to manually solve the expression of f_x and k_p with GM. Therefore, the restriction of GM at f_x can be transformed into the restriction on the magnitude (defined as $-GM_r$) of $G_{op3}(s)$ at f_r. Thus, GM_r can be expressed as

$$GM_r = GM - \Delta GM_2. \tag{30}$$

The magnitude of $G_{op3}(s)$ at f_r can be derived as

$$\left| G_{op3}(j\omega)|_{\omega=2\pi f_r} \right| = \frac{2k_p\sqrt{(1+\omega_r^2 R_d^2 C^2)}}{\omega_r^2 R_d C(L_1+L_2)}. \tag{31}$$

With the definition of GM_r, GM_r can also be derived as

$$GM_r = -20\log_{10}\left| G_{op3}(j\omega)|_{\omega=2\pi f_r} \right|. \tag{32}$$

By substituting (30) and (31) into (32), k_p under a restriction of GM can be derived as

$$k_{p\_GM} = \frac{\omega_r^2 R_d C(L_1+L_2)10^{-(GM-\Delta GM_2)/20}}{2\sqrt{1+\omega_r^2 R_d^2 C^2}} \tag{33}$$

where ΔGM_2 is approximately equal to the ΔGM_1 of $G_{op3}(s)$ without PI controller. As for ΔGM_1, it can be determined in advance in Fig. 10.

Then, the smaller one of k_{p_PM} and k_{p_GM} is selected as the final proportional parameter k_p, which can make the PM and GM be satisfied at the same time. Therefore, k_p is designed as

$$k_p = \min\{k_{p\_PM}, k_{p\_GM}\}. \tag{34}$$

Finally, the PI control parameter can be easily determined by (23) and (34), without multiple iterations of design. Therefore, under the appropriate PM and GM settings, this designed PI control parameter can make the proposed SDDSCC scheme achieve a good stability, and a fast current dynamic response, and a high robustness.

C. Performance Comparison

According to [36], the specifications of open-loop transfer function are given as follows: PM $\geq 45°$ and GM ≥ 5 dB, which can ensure a good dynamic performance and an enough stability margin. In this article, the expected PM is set to 65° and the minimum GM is also set to 5 dB. The circuit parameters are given in Table I. With the expected PM and the restriction of GM, the PI parameter of proposed SDDSCC can thus be determined according to (23) and (34), and the result is given in Table II. Then, the bode diagram of SDDSCC can be plotted in Fig. 11. As seen, PM is 67.7° and GM is 9.66 dB and both of them meet the expected stability margin.

By referring to [35], the PI parameter of conventional DSCC with NF under the expected PM and GM can be designed and the result is given in Table II. The bode diagram is plotted in Fig. 12(a). From Figs. 11 and 12(a), it can be seen that the bandwidth of the proposed SDDSCC (2230 rad/s) is 18 times that of the conventional DSCC with NF (121 rad/s) under the same PM (68° around). If the bandwidth of conventional DSCC with NF is widened, the PM needs to be decreased. In this case, another PI parameter with the expected PM 35° is designed and the result is also shown in Table II, and the bode diagram is shown in Fig. 12(b). From Figs. 11 and 12(b), it can be seen that bandwidth of proposed SDDSCC (2230 rad/s) is still 6.6 times that of the conventional DSCC with NF (340 rad/s) in this case. Therefore, the proposed SDDSCC will have a faster current dynamic response.

TABLE II
PARAMETERS OF THE CONTROLLERS

Scheme	PM	k_p	k_i	bandwidth
Conventional DSCC with NF	35.5°	0.8	20	340 rad/s
	68.4°	0.2	2	121 rad/s
Proposed SDDSCC	67.7°	1.75	315.8	2230 rad/s

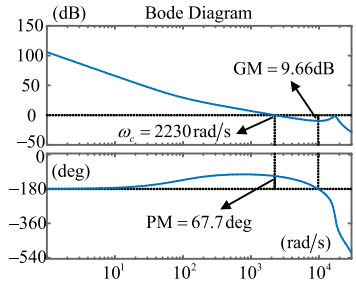

Fig. 11. Bode diagram of the proposed SDDSCC, PM = 67.7°.

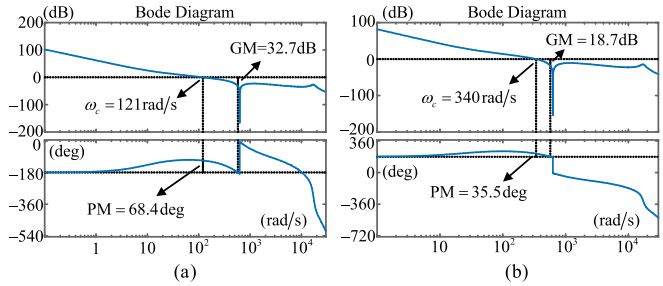

Fig. 12. Bode diagram of the conventional DSCC with NF. (a) PM = 68.4°, (b) PM = 35.5°.

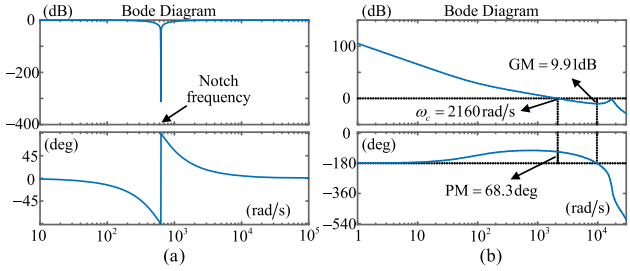

Fig. 13. (a) Bode diagram of NF, (b) bode diagram of $G_{\mathrm{op1}}(s)$ without NF under PM = 68.3°.

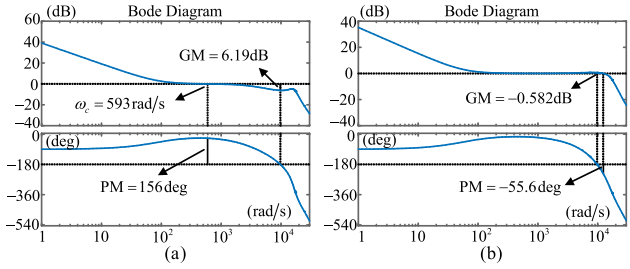

Fig. 14. Bode diagram of $G_{\mathrm{op2}}(s)$. (a) $k_p = 3.5$. (b) $k_p = 5.5$.

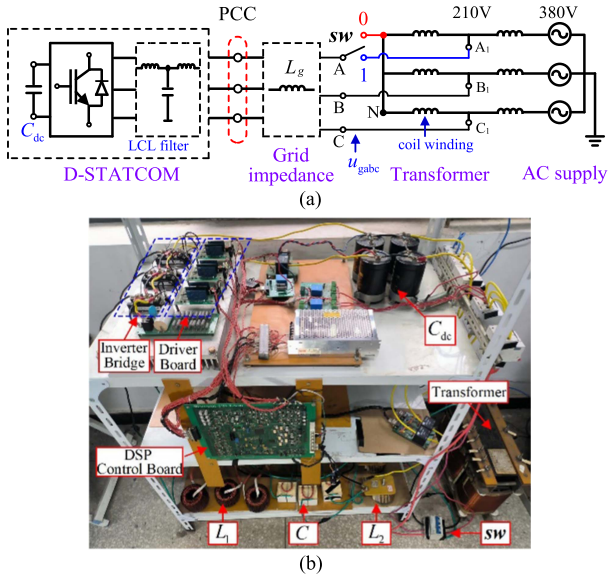

Fig. 15. (a) Schematic diagram and (b) photograph of experimental setup.

IV. Experimental Results

The schematic diagram and photograph of the experimental setup are shown in Fig. 15(a) and (b), respectively. The circuit parameters are given in Table I. The controller parameters of the proposed scheme and conventional scheme are given in Table II.

In Fig. 15, by switching the breaker ***sw*** to tap 0 of the transformer, a seriously single-line-to-ground grid fault is created that A-phase grid voltage u_{ga} drops to zero. u_{gb} and u_{gc} remain unchanged. In this case, the grid phase voltage is shown in Fig. 16. After sequence analysis, the positive sequence voltage decreases to 65.5% of the rated voltage and the negative sequence voltage rises to 32.9%.

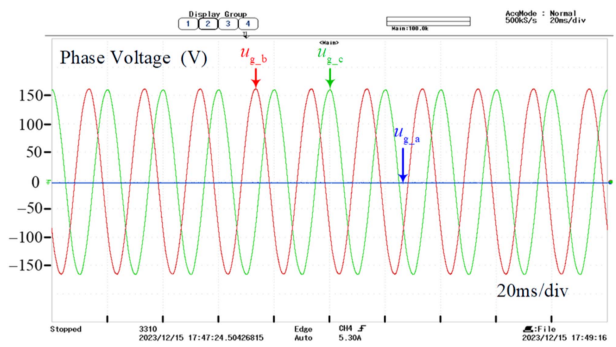

Fig. 16. Unbalanced grid phase voltage for experiment.

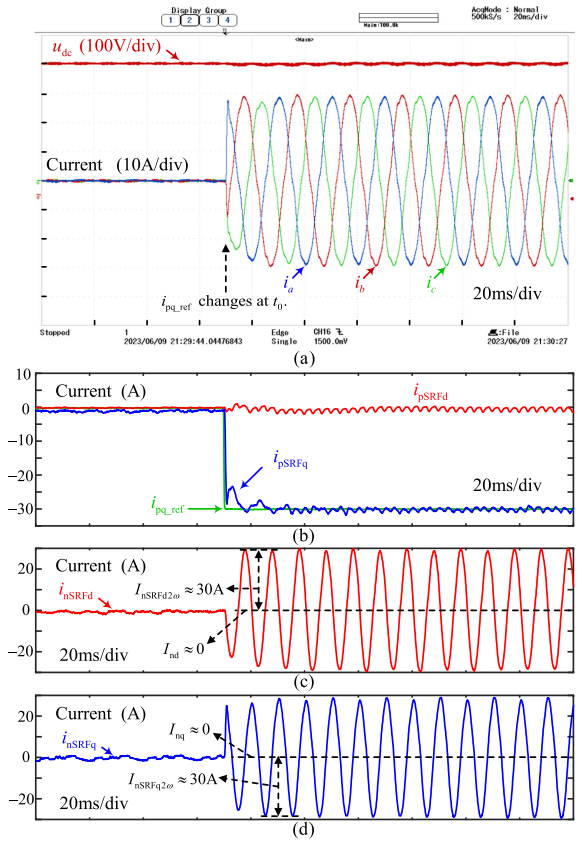

Fig. 17. Experimental result of proposed SDDSCC under the step-up of i_{pq_ref}.

Under the unbalanced grid voltage shown in Fig. 16, two kinds of current reference step-ups are set to evaluate the performance of the proposed SDDSCC scheme.

A. *Step-Up of Positive Sequence* q*-Axis Current Reference*

A step-up of single positive sequence q-axis current reference is set from 0 to −30 A. The experimental results of the proposed SDDSCC and the conventional DSCC with PM 68.4° are presented in Figs. 17 and 18, respectively. In order to evaluate the dynamic performance of the control schemes under a serious situation, the current reference step-up moment t_0 of each experiment is selected at the A-phase current peak.

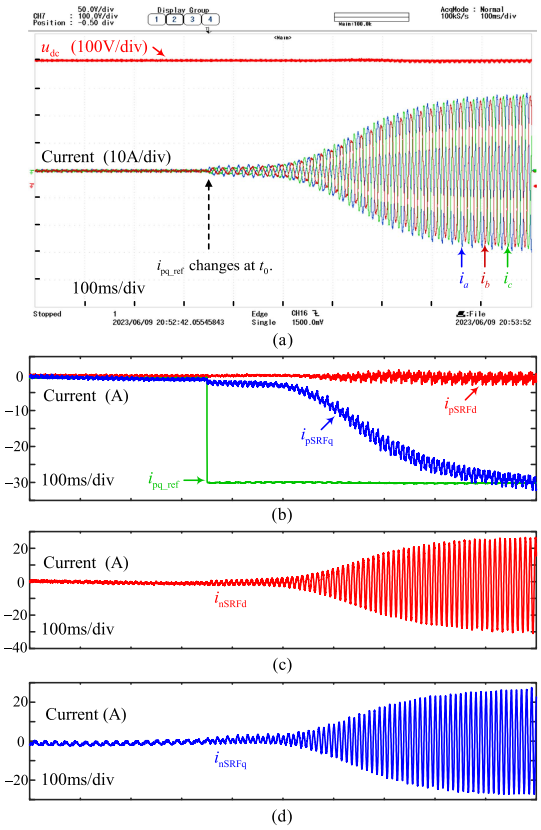

Fig. 18. Experimental result of the conventional DSCC with PM 68.4° under the step-up of i_{pq_ref}.

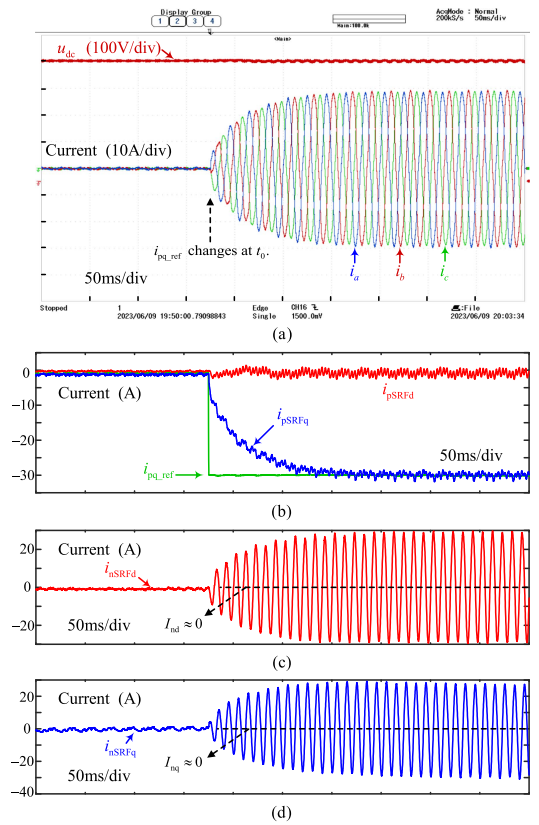

Fig. 19. Experimental result of the conventional DSCC with PM 35.5° under the step-up of i_{pq_ref}.

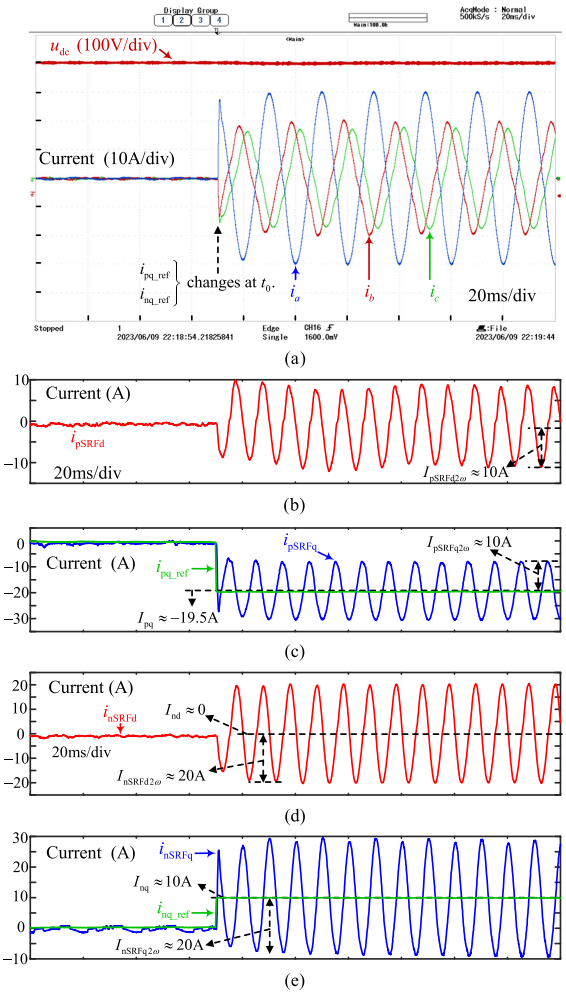

Fig. 20. Experimental result of the proposed SDDSCC under the step-up of i_{pq_ref} and i_{nq_ref}.

The steady-state result under the proposed SDDSCC is three-phase balanced current and the current peak also reaches expected 30 A, as shown in Fig. 17(a). From i_{abc} and i_{pSRFq} in Fig. 17(a) and (b), it can be seen that the current under the proposed SDDSCC can quickly track the reference without overshoot after the reference step-up. The response time is within 20 ms around. Besides, the *dq* coupling ripple of i_{pSRFd} at t_0 caused by the abrupt step-up of i_{pSRFq} is also quite small. It indicates the *dq* current decoupling is achieved by the proposed SDDSCC.

In Fig. 17(c) and (d), i_{nSRFd} and i_{nSRFq} contain only the second harmonic components (i.e., $i_{nSRFd2\omega}$ and $i_{nSRFq2\omega}$) as expected. The amplitudes of them are the same, i.e., $I_{nSRFd2\omega} \approx I_{nSRFq2\omega} \approx 30$ A, as expected. Besides, the fast current response and the good *dq* decoupling effect under the proposed SDDSCC can be indirectly reflected by the envelope curve of i_{nSRFd} or i_{nSRFq}.

With the same PM 68° as SDDSCC, the current response of the conventional DSCC with NF under the step-up of i_{pq_ref} is presented in Fig. 18. The response time is about 600 ms, which is about 30 times that of the proposed SDDSCC.

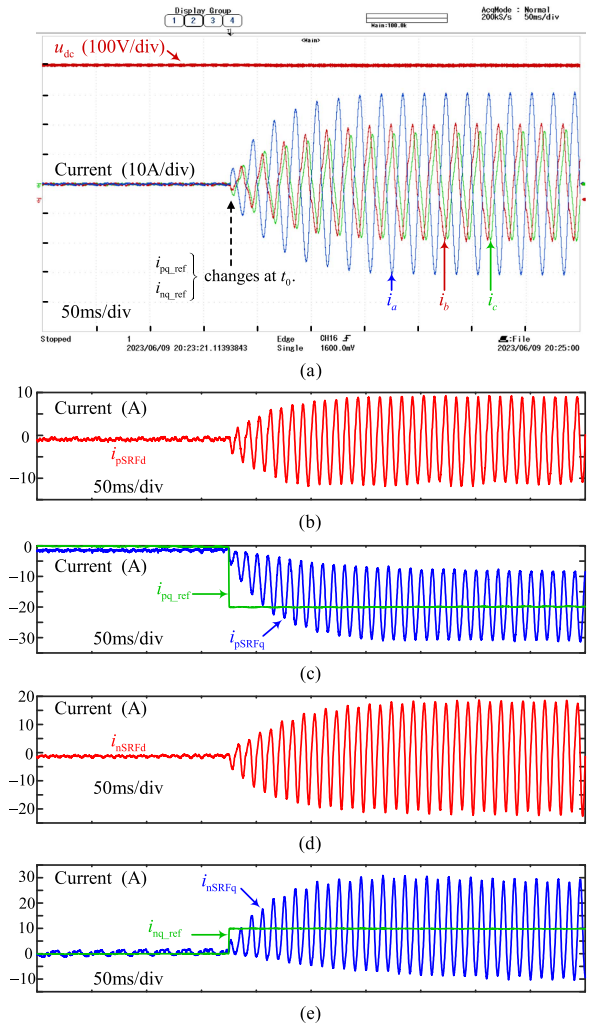

Fig. 21. Experimental result of the conventional DSCC with PM 35.5° under the step-up of i_{pq_ref} and i_{nq_ref}.

If the response of the conventional DSCC with NF needs to be accelerated, another PI parameter with the expected PM 35° is designed and given in Table II. In this case, the experimental result can be shown in Fig. 19. It can be seen that the response time is about 130 ms, which is still about 6.5 times that of the proposed SDDSCC in Fig. 17.

B. Step-Up of Positive and Negative Sequence q*-Axis Current References*

The positive and negative sequence q-axis current reference i_{pq_ref}, i_{nq_ref} step up at t_0 simultaneously. i_{pq_ref} steps up from 0 to −20 A and i_{nq_ref} is from 0 to 10 A. The experimental results of the proposed SDDSCC and the conventional DSCC with PM 35.5° are presented in Figs. 20 and 21, respectively.

In Fig. 20(b)–(e), the steady-state I_{pq} of the dc component of $i_{pSRF\,q}$ is about −19.5 A and the steady-state I_{nq} of the dc component of $i_{nSRF\,q}$ is about 10 A, which indicates the steady-state control objectives of i_{pq_ref} and i_{nq_ref} are well achieved. Furthermore, from i_{abc} and $i_{pSRF\,d}$, etc., it can be seen that the response time is about 20 ms without overshoot, similar to that of Fig. 17. Besides, both the *dq* coupling ripples of the dc components of $i_{pSRF\,d}$ and $i_{nSRF\,d}$ caused by the sudden step-up of i_{pq_ref} and i_{nq_ref} are also quite small, verifying the good *dq* current decoupling effect of the proposed SDDSCC.

Contrastively, from Fig. 21, it can be seen that the current response time of the conventional DSCC with NF and PM 35.5° under the step-up of i_{pq_ref} and i_{nq_ref} is 130 ms around, which is close to the result of Fig. 19 as expected.

To clearly compare the experimental results, a given Table III is established. It can be summarized from the Table III that the proposed SDDSCC scheme has a faster current dynamic

TABLE III
SUMMARY OF EXPERIMENTAL RESULTS

Schemes	PM	Need SE	Need specialized dq decoupling	Step-up of i_{pq_ref}		Step-up of i_{pq_ref} and i_{nq_ref}	
				Response time	THD of i_{abc}	Response time	THD of i_{abc}
SDDSCC	67.7deg	No	No	20 ms	4.3%	20 ms	4.32%
Conventional DSCC with NF	68.4deg	Yes	Yes	600 ms	6.45%	—	—
	35.5deg			130 ms	5.5%	130 ms	6.2%

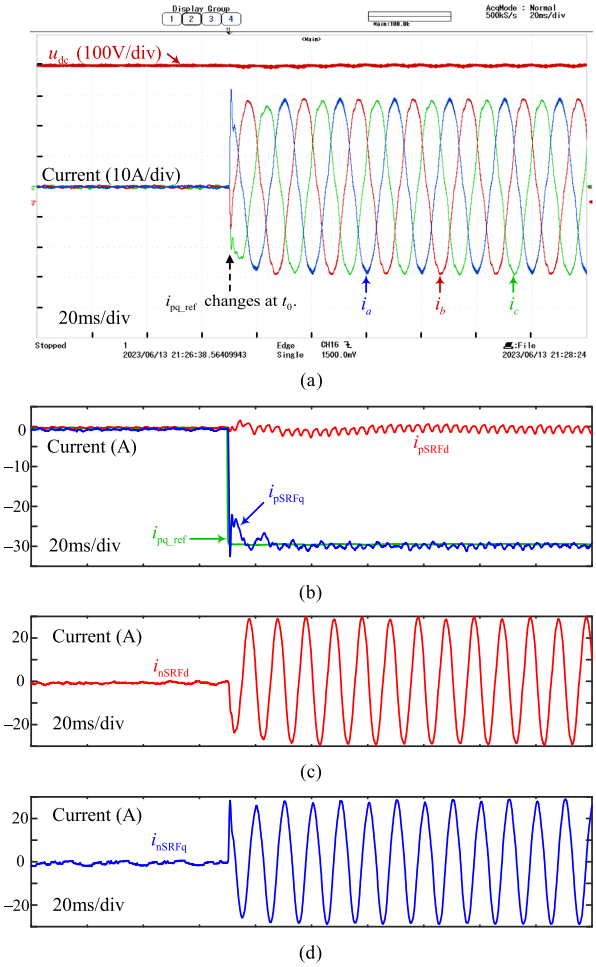

Fig. 22. Experimental result of the proposed SDDSCC under $0.75L_1$, $0.66C$, and $0.5L_2$, with the step-up of i_{pq_ref}.

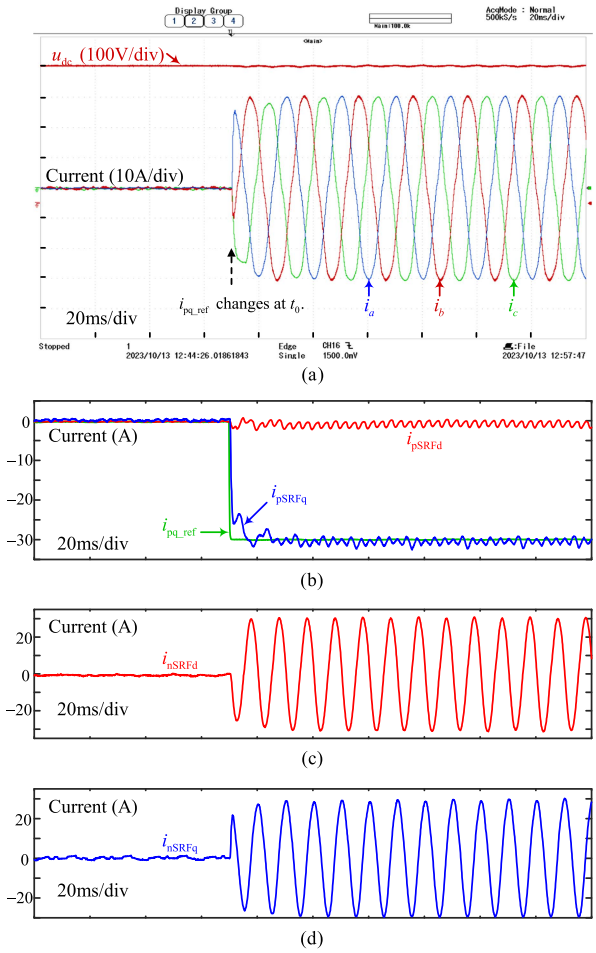

Fig. 23. Experimental result of the proposed SDDSCC under $1.5L_1$, $1.33C$, and $1.66L_2$, with the step-up of i_{pq_ref}.

response than the conventional DSCC scheme with NF under different operation conditions. Besides, the proposed SDDSCC does not require SE or specialized *dq* current decoupling method, showing the simpler control structure. The total harmonic distortion (THD) of the steady-state current under SDDSCC is smaller, which is due to the larger control bandwidth of the SDDSCC.

C. *SDDSCC Under Parameter Shift of* LCL

To evaluate the performance of proposed SDDSCC under the filter *LCL* parameter shift, two cases are set. The first case is that L_1, C and L_2 are reduced to 75%, 66.6% and 50% of the rated value, respectively. The second is that L_1, C and L_2 are increased to 150%, 133.3%, and 166%, respectively. Under the step-up of i_{pq_ref}, the experimental results of the proposed SDDSCC in the above two cases are shown in Figs. 22 and 23, respectively. It can be seen that the current response time for both cases is 23 ms around, which is slightly longer than that of Fig. 17 in normal *LCL* situation. Nevertheless, the stability for both cases is not affected by the abnormal *LCL* shifts. Besides, both the steady-state results under the above two cases are three-phase balanced current and the current peaks also reach expected 30 A.

Figs. 22 and 23 show the experimental results of proposed scheme when the *LCL* parameter is shifted to lower and higher,

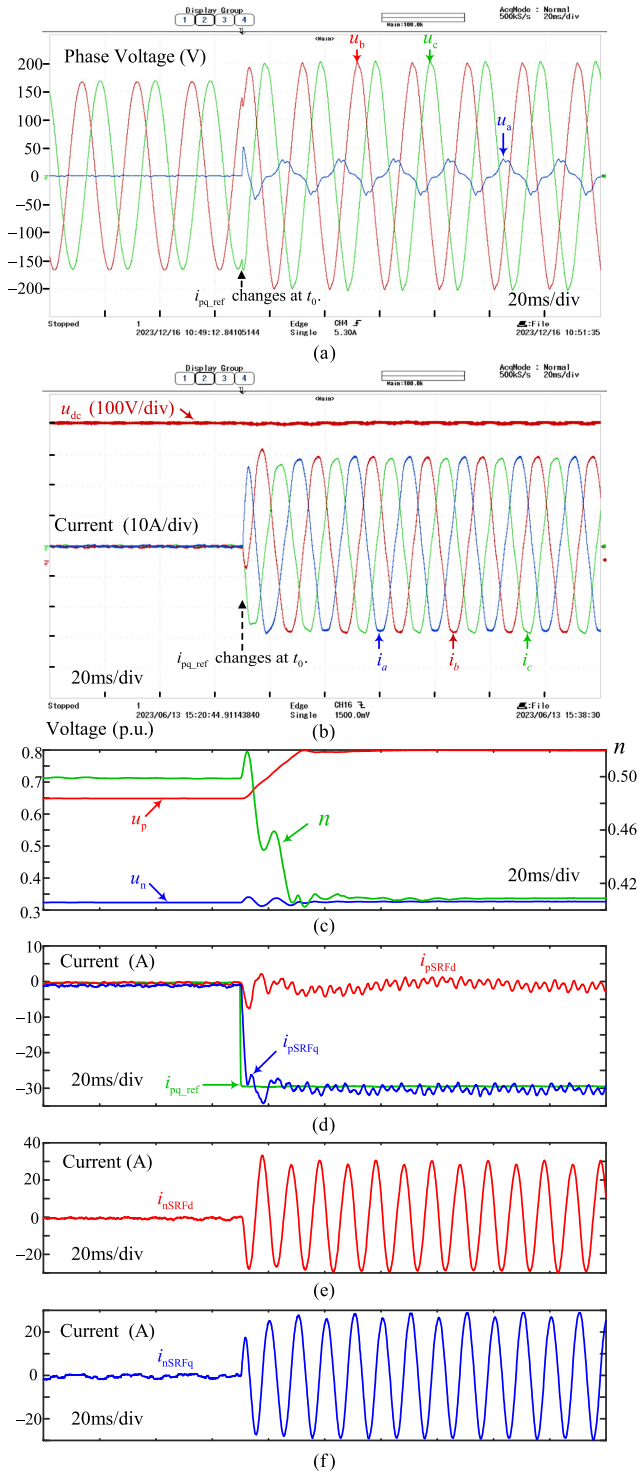

Fig. 24. Experimental result of the proposed SDDSCC under the weak grid (i.e., SCR = 5.2), with the step-up of i_{pq_ref}.

respectively. It is seen that the stability, steady-state and dynamic performances are not greatly affected.

Therefore, the proposed SDDSCC scheme can still achieve a good current control performance under a large range of *LCL* parameter shift, regardless of whether it is towards lower or higher. This verifies the high robustness of proposed SDDSCC scheme.

D. SDDSCC Under Weak Grid

To evaluate the performance of proposed SDDSCC under the weak grid, an inductance of 3.0 mH is connected in series into the grid circuit. Thus, L_g becomes 3.45 mH, i.e., short-circuit ratio (SCR) is 5.2 around.

Then, with the step-up of i_{pq_ref}, the experimental result of SDDSCC under the weak grid is shown in Fig. 24. From the responses of i_{abc} and $i_{p\mathrm{SRF}\,q}$ etc., it can be seen that the current can still quickly track the reference without large overshoot, and the current response time is around 22 ms. This result is similar to that of Fig. 17 in the strong grid. Therefore, the proposed SDDSCC can be well adopted in the weak grid, with good control stability and current response.

In the case of a weak grid, the PCC voltage will be affected by the output current of D-STATCOM according to circuit theory. The PCC phase voltage waveform is shown in the subfigure (a). It can be seen that each phase voltage is boosted to a certain extent after the step-up change of i_{pq_ref}. The positive sequence voltage u_p is boosted to 80% of the rated voltage from 65.5%, and the negative sequence voltage u_n remains unchanged at 32.9%, as seen in the subfigure (c). This is because the D-STATCOM only injects positive sequence reactive current into the grid in this case. Accordingly, the unbalance degree n ($n = u_n/u_p$) decreases to 0.41 from 0.5.

V. Conclusion

In this article, an SDDSCC scheme based on double SRF is proposed for D-STATCOM when it suffers from an unbalanced grid voltage. Accordingly, a novel control parameter design method of the SDDSCC is also proposed. The proposed SDDSCC can achieve two types of decoupling. One is the positive and negative sequence current decoupling in double SRF without SE. The other is the *dq* current decoupling without specialized *dq* current decoupling method. Due to not using the SE and specialized *dq* decoupling method, the control bandwidth of the proposed SDDSCC is larger and the current dynamic response is faster, and the control structure and the implementation are simpler, compared to the conventional control schemes with SE. Besides, the control parameter can be easily determined by the proposed novel control parameter design method without multiple iterations of design.

The proposed SDDSCC scheme can also be applied to general photovoltaic inverters and wind power converters when they need to inject unbalanced current into the grid, e.g., load balancing or LVRT under unbalanced grid faults. Besides, how to apply the proposed SDDSCC to the unbalanced voltage closed-loop control is a worthwhile research direction in the future. In addition, how to achieve a complete *dq* decoupling (also including ωC, besides ωL_1 and ωL_2) of the SDDSCC also needs to be further studied.

References

[1] N. G. Hingorani and L. Gyugyi, "Static shunt compensators: SVC and STATCOM," in *Understanding FACTS: Concepts and Technology of Flexible AC Transmission Systems*. Piscataway, NJ, USA: Wiley, 2000, pp. 135–207.

[2] R. K. Varma, S. A. Rahman, and T. Vanderheide, "New control of PV solar farm as STATCOM (PV-STATCOM) for increasing grid power transmission limits during night and day," *IEEE Trans. Power Del.*, vol. 30, no. 2, pp. 755–763, Apr. 2015.

[3] M. Molinas, J. A. Suul, and T. Undeland, "Low voltage ride through of wind farms with cage generators: STATCOM versus SVC," *IEEE Trans. Power Electron.*, vol. 23, no. 3, pp. 1104–1117, May 2008.

[4] G. Li, Y. Chen, A. Luo, and H. Wang, "An enhancing grid stiffness control strategy of STATCOM/BESS for damping sub-synchronous resonance in wind farm connected to weak grid," *IEEE Trans. Ind. Inform.*, vol. 16, no. 9, pp. 5835–5845, Sep. 2020.

[5] T. Neumann, T. Wijnhoven, G. Deconinck, and I. Erlich, "Enhanced dynamic voltage control of type 4 wind turbines during unbalanced grid faults," *IEEE Trans. Energy Convers.*, vol. 30, no. 4, pp. 1650–1659, Dec. 2015.

[6] C. Li, S. K. Chaudhary, M. Savaghebi, J. C. Vasquez, and J. M. Guerrero, "Power flow analysis for low-voltage ac and dc microgrids considering droop control and virtual impedance," *IEEE Trans. Smart Grid*, vol. 8, no. 6, pp. 2754–2764, Nov. 2017.

[7] J. Jia, G. Yang, and A. H. Nielsen, "A review on grid-connected converter control for short-circuit power provision under grid unbalanced faults," *IEEE Trans. Power Del.*, vol. 33, no. 2, pp. 649–661, Apr. 2018.

[8] X. Zhao, J. M. Guerrero, M. Savaghebi, J. C. Vasquez, X. Wu, and K. Sun, "Low-Voltage ride-through operation of power converters in grid-interactive microgrids by using negative-sequence droop control," *IEEE Trans. Power Electron.*, vol. 32, no. 4, pp. 3128–3142, Apr. 2017.

[9] *Technical Requirements for Wind Power and Photovoltaic Installations and any Generating Facilities Whose Technology Does not Consist on A Synchronous Generator Directly Connected to the Grid*, Offprint of the Operation Procedure O.P. 12.2, Asociación Empresarial Eólica, Madrid, Spain, Oct. 2008.

[10] *Grid Code—High and Extra High Voltage*, E.ON Netz GmbH, Bayreuth, Germany, Apr. 2006.

[11] *Wind Turbines Connected to Grids with Voltages below 100 kV*, Regulation TF 3.2.6, Energinet, Denmark, May 2004.

[12] "Technical requirements for the connection and operation of customer installations to the medium-voltage network (TCC medium-voltage)," VDE, Germany, Tech. Rep. VDE-AR-N 4110, Feb. 2017.

[13] M. G. Taul, X. Wang, P. Davari, and F. Blaabjerg, "Current reference generation based on next-generation grid code requirements of grid-tied converters during asymmetrical faults," *IEEE J. Emerg. Sel. Topics Power Electron.*, vol. 8, no. 4, pp. 3784–3797, Dec. 2020.

[14] X. Wang and L. Peng, "Dynamic voltage equalization control of D-STATCOM under unbalanced grid faults in a low-voltage network," *IEEE Trans. Power Electron.*, vol. 38, no. 2, pp. 2384–2397, Feb. 2023.

[15] X. Guo, W. Liu, and Z. Lu, "Flexible power regulation and current-limited control of the grid-connected inverter under unbalanced grid voltage faults," *IEEE Trans. Ind. Electron.*, vol. 64, no. 9, pp. 7425–7432, Sep. 2017.

[16] T. Lee, S. Hu, and Y. Chan, "D-STATCOM with positive-sequence admittance and negative-sequence conductance to mitigate voltage fluctuations in high-level penetration of distributed-generation systems," *IEEE Trans. Ind. Electron.*, vol. 60, no. 4, pp. 1417–1428, Apr. 2013.

[17] A. Khoshooei, J. S. Moghani, I. Candela, and P. Rodriguez, "Control of D-STATCOM during unbalanced grid faults based on dc voltage oscillations and peak current limitations," *IEEE Trans. Ind. Appl.*, vol. 54, no. 2, pp. 1680–1690, Mar./Apr. 2018.

[18] T. Ye, N. Dai, C.-S. Lam, M.-C. Wong, and J. M. Guerrero, "Analysis, design, and implementation of a quasi-proportional-resonant controller for a multifunctional capacitive-coupling grid-connected inverter," *IEEE Trans. Ind. Appl.*, vol. 52, no. 5, pp. 4269–4280, Sep./Oct. 2016.

[19] D. N. Zmood and D. G. Holmes, "Stationary frame current regulation of PWM inverters with zero steady-state error," *IEEE Trans. Power Electron.*, vol. 18, no. 3, pp. 814–822, May 2003.

[20] J. Hu, H. Xu, and Y. He, "Coordinated control of DFIG's RSC and GSC under generalized unbalanced and distorted grid voltage conditions," *IEEE Trans. Ind. Electron.*, vol. 60, no. 7, pp. 2808–2819, Jul. 2013.

[21] Y. Hu, Z. Q. Zhu, and M. Odavic, "Instantaneous power control for suppressing the second-harmonic DC-bus voltage under generic unbalanced operating conditions," *IEEE Trans. Power Electron.*, vol. 32, no. 5, pp. 3998–4006, May 2017.

[22] A. Sahoo, J. Ravishankar, M. Ciobotaru, and F. Blaabjerg, "Enhanced fault ride-through of power converters using hybrid grid synchronization," *IEEE J. Emerg. Sel. Topics Power Electron.*, vol. 10, no. 3, pp. 2829–2841, Jun. 2022.

[23] H. - S. Song and K. Nam, "Dual current control scheme for PWM converter under unbalanced input voltage conditions," *IEEE Trans. Ind. Electron.*, vol. 46, no. 5, pp. 953–959, Oct. 1999.
[24] M. A. Azzouz and A. Hooshyar, "Dual current control of inverter-interfaced renewable energy sources for precise phase selection," *IEEE Trans. Smart Grid*, vol. 10, no. 5, pp. 5092–5102, Sep. 2019.
[25] G. Amico, A. Egea-Àlvarez, P. Brogan, and S. Zhang, "Small-signal converter admittance in the *pn*-frame: Systematic derivation and analysis of the cross-coupling terms," *IEEE Trans. Energy Convers.*, vol. 34, no. 4, pp. 1829–1838, Dec. 2019.
[26] S.-Z. Chen, J. Lu, G. Zhang, and Y. Zhang, "Immunizing variable frequency transformer from dual-side asymmetrical grid faults via a single-converter-based novel control strategy," *IEEE Trans. Power Del.*, vol. 35, no. 3, pp. 1330–1338, Jun. 2020.
[27] M. Cheng, X. Yan, and J. Zhou, "Negative-sequence current compensation-based coordinated control strategy for dual-cage-rotor brushless doubly fed induction generator under unbalanced grid conditions," *IEEE Trans. Ind. Electron.*, vol. 70, no. 5, pp. 4762–4773, May 2023.
[28] A. T. Nguyen and D.-C. Lee, "Advanced grid synchronization scheme based on dual eSOGI-FLL for grid-feeding converters," *IEEE Trans. Power Electron.*, vol. 37, no. 6, pp. 7218–7229, Jun. 2022.
[29] A. Meligy, T. Qoria, and I. Colak, "Assessment of sequence extraction methods applied to MMC-SDBC STATCOM under distorted grid conditions," *IEEE Trans. Power Del.*, vol. 37, no. 6, pp. 4923–4932, Dec. 2022.
[30] J. Hu and Y. He, "Reinforced control and operation of DFIG-based wind-power-generation system under unbalanced grid voltage conditions," *IEEE Trans. Energy Convers.*, vol. 24, no. 4, pp. 905–915, Dec. 2009.
[31] M. Reyes, P. Rodriguez, S. Vazquez, A. Luna, R. Teodorescu, and J. M. Carrasco, "Enhanced decoupled double synchronous reference frame current controller for unbalanced grid-voltage conditions," *IEEE Trans. Power Electron.*, vol. 27, no. 9, pp. 3934–3943, Sep. 2012.
[32] S. Zhou, J. Liu, L. Zhou, and H. She, "Dual sequence current controller without current sequence decomposition implemented on DSRF for unbalanced grid voltage conditions," in *Proc. IEEE Energy Convers. Congr. Expo.*, 2014, pp. 60–67.
[33] R. Kabiri, D. G. Holmes, and B. P. McGrath, "Double synchronous frame current regulation of distributed generation systems under unbalanced voltage conditions without sequence current separation," in *Proc. Appl. Power Electron. Conf. Expo.*, 2015, pp. 1822–1829.
[34] J. Lei, B. Zhou, J. Bian, X. Qin, and J. Wei, "A simple method for sinusoidal input currents of matrix converter under unbalanced input voltages," *IEEE Trans. Power Electron.*, vol. 31, no. 1, pp. 21–25, Jan. 2016.
[35] S. Zhou et al., "An improved design of current controller for *LCL*-type grid-connected converter to reduce negative effect of PLL in weak grid," *IEEE J. Emerg. Sel. Topics Power Electron.*, vol. 6, no. 2, pp. 648–663, Jun. 2018.
[36] C. Bao, X. Ruan, X. Wang, W. Li, D. Pan, and K. Weng, "Step-by-step controller design for *LCL*-type grid-connected inverter with capacitor–current-feedback active-damping," *IEEE Trans. Power Electron.*, vol. 29, no. 3, pp. 1239–1253, Mar. 2014.
[37] D. Pan, X. Ruan, C. Bao, W. Li, and X. Wang, "Capacitor-current-feedback active damping with reduced computation delay for improving robustness of *LCL*-type grid-connected inverter," *IEEE Trans. Power Electron.*, vol. 29, no. 7, pp. 3414–3427, Jul. 2014.
[38] P. RodrÍguez, A. Timbus, R. Teodorescu, M. Liserre, and F. Blaabjerg, "Reactive power control for improving wind turbine system behavior under grid faults," *IEEE Trans. Power Electron.*, vol. 24, no. 7, pp. 1798–1801, Jul. 2009.
[39] R. Kabiri, D. G. Holmes, and B. P. McGrath, "Control of active and reactive power ripple to mitigate unbalanced grid voltages," *IEEE Trans. Ind. Appl.*, vol. 52, no. 2, pp. 1660–1668, Mar./Apr. 2016.
[40] X. Guo, S. Du, N. Diao, C. Hua, and F. Blaabjerg, "Three-dimensional space vector modulation for four-leg current-source inverters," *IEEE Trans. Power Electron.*, vol. 38, no. 10, pp. 13122–13132, Oct. 2023.

Xuefeng Wang received the B.Eng. degree in electrical engineering and automation from North China University of Water Resources and Electric Power, Zhengzhou, China, in 2013.

He is currently working toward the Ph.D. degree with the School of Electrical and Electronic Engineering, Huazhong University of Science and Technology. His major research interests include the control and analysis of power electronic converter.

Li Peng (Senior Member, IEEE) received the B.S., M.S., and Ph.D. degrees from the Huazhong University of Science and Technology (HUST), Wuhan, China, in 1989, 1992, and 2004, respectively, all in electrical engineering.

In 1992, she was with the HUST, where she is currently a Full Professor with the School of Electrical and Electronic Engineering. Her research interests include power electronic conversion, its control and applications, modular power supply and parallel control technique, renewable energy generation, power quality control, and MMC for HVdc applications.